

Sub-100-fs formation of dark excitons in monolayer WS_2

Pavel V. Kolesnichenko,^{*,†,‡} Lukas Wittenbecher,[¶] Qianhui Zhang,[⊥] Run Yan
Teh,[#] Chandni Babu,[§] Michael S. Fuhrer,^{@,Δ} Anders Mikkelsen,[¶] and Donatas
Zigmantas^{*,§}

[†]*Institute of Physical Chemistry, Heidelberg University, 69120, Heidelberg, Germany*

[‡]*Institute for Molecular Systems, Engineering and Advanced Materials, Heidelberg
University, 69120, Heidelberg, Germany*

[¶]*Department of Physics, Lund University, Box 118, 221 00 Lund, Sweden*

[§]*Division of Chemical Physics, Lund University, P.O. Box 124, 221 00 Lund, Sweden*

^{||}*NanoLund, P.O. Box 124, 221 00 Lund, Sweden*

[⊥]*Department of Civil Engineering, Monash University, Melbourne, Victoria 3800,
Australia*

[#]*Centre for Quantum Science and Technology Theory, Swinburne University of
Technology, Melbourne, Victoria 3122, Australia*

[@]*School of Physics and Astronomy, Monash University, Melbourne, Victoria 3800,
Australia*

^Δ*ARC Centre of Excellence in Future Low-Energy Electronics Technologies, Monash
University, Melbourne, Victoria 3800 Australia*

E-mail: pavel.kolesnichenko@alumni.uni-heidelberg.de; donatas.zigmantas@chemphys.lu.se

Abstract

Two-dimensional semiconductors based on transition metal dichalcogenides are promising for electronics and optoelectronics applications owing to their properties governed by strongly-bound bright and dark excitons. Momentum-forbidden dark excitons have recently received attention as better alternatives to bright excitons for long-range transport. However, accessing the dynamics of dark excitons is challenging experimentally. The most direct, but very complicated, experiment is transient angle-resolved photoemission electron spectroscopy: sub-100-*fs* formation of K- Λ -excitons in monolayer WS₂ has been identified previously taking advantage of momentum resolution of detected signals.¹ Here, we use a simpler setting of transient photoemission electron microscopy (with spatial resolution of 75 nm), which is inherently sensitive to dark K- Λ excitons in monolayers of transition metal dichalcogenide and has exceptionally high temporal resolution of 13 fs. We are able to directly observe intervalley scattering (dark-exciton formation) in monolayer WS₂ with scattering rates in the range of 14–50 *fs* followed by picosecond-scale dynamics mediated by defects.

Keywords

WS₂, monolayer, excitons, 2D materials, transition metal dichalcogenide, intervalley scattering, femtosecond, microscopy, PEEM, pump-probe, semiconductor

Introduction

Two-dimensional (2D) semiconductors such as monolayers of transition metal dichalcogenide (TMdC) are promising for numerous applications in optics and optoelectronics because they provide rich exciton physics.² Large exciton binding energies of ~ 0.5 eV in these materials make 2D excitons stable even at room temperature, which allows achieving high exciton densities.³ This has enabled observations of various exciton formations such as neutral⁴ and

charged⁵ excitons, bi-excitons,⁶ and higher-order exciton complexes.⁷ This, in turn, renders TMdC monolayers an ideal platform for investigations of various many-body interactions and related emerging phenomena.^{8–12}

Zero-momentum direct excitons in TMdC monolayers form in K valleys of the Brillouin zone, facilitated by enhanced electron-hole Coulomb interactions.¹³ Subsequent scattering of these excitons to adjacent valleys leads to strongly-bound dark excitons.¹ Due to their net non-zero momentum, dark excitons have recently received much attention as quasi-particles that could be better alternatives to bright excitons when it comes to long-range transport.^{14–17} Accessing momentum-forbidden dark excitations, however, is an experimental challenge: optical spectroscopy is not capable of their direct probing, and momentum-resolved photoemission spectroscopy, although capable of direct detection of intervalley carriers, is experimentally highly challenging.

Numerous studies reported on the life-cycle of bright and dark 2D excitons in a variety of experimental settings covering their formation,^{18–20} ultrafast cooling,²¹ intervalley scattering,^{1,22–24} and ultimate fate (*e.g.*, exciton-exciton annihilation,^{25–27} electron-hole recombination,²⁷ and exciton dissociation²⁸). Exciton cooling, formation, and intervalley scattering are amongst initial processes occurring on femtosecond timescales²⁹ with the fastest reported being on a sub-100 *fs* time scale.^{20,22,23} Therefore, in studying dark excitons, an additional challenge of resolving early-stage dynamics has to also be overcome – advanced ultrafast spectroscopy techniques with very high temporal resolution are required. Optimizing the temporal resolution becomes even more crucial in cases when exciton dynamics occur on a sub-100-*fs* time scale. However, pushing the resolution of femtosecond photoemission-based apparatus to the level needed for confident identification of sub-100-*fs* ultrafast processes poses a formidable challenge.

Femtosecond carrier kinetics in 2D semiconductors have previously been identified using optical pump-probe spectroscopy,^{18–20} time-resolved photoemission electron microscopy (TR-PEEM),^{21,23,30–33} and transient angle-resolved photoemission electron spectroscopy (TR-

ARPES).^{1,22,34} Sub-100-*fs* dynamics has been recognized in other related materials as well, *e.g.*, bilayer MoSe₂ (~ 54 *fs*) from lineshapes acquired via 2D electronic spectroscopy,³⁵ and bulk WSe₂ (60–70 *fs*,³⁶ ~ 17 *fs*³⁷) through TR-ARPES. The time-resolution in all of these experiments, however, was in the range of ~ 20 –200 *fs* with the most common value of a few tens of femtoseconds. Here, we pushed the resolution below 20 *fs* enabling direct observation of intervalley carrier dynamics in the temporal domain.

More specifically, in this study, we combine photoemission electron microscopy (PEEM) with high spatial resolution (75 *nm*) and femtosecond pump-probe spectroscopy with exceptionally high temporal resolution (13 *fs*). Pumping at the main exciton resonance (2 *eV*), we study subsequent carrier dynamics in WS₂ monolayer using the developed transient PEEM (TR-PEEM) apparatus. By design of the experiment, we detect ultrafast intervalley scattering from K valleys (*i.e.*, formation of dark excitons) occurring with a time constant in the range of 14 – 50 *fs*, detected via photoemission stimulated by broadband probe pulses in the deep-ultraviolet (DUV, 4.7 *eV*). A high-temporal resolution was ultimately achieved by generation of very short DUV pulses via achromatic phase matching in a nonlinear crystal, described previously^{38,39} but never used before as part of transient photoemission microscopes.

In monolayers, sub-100-*fs* carrier dynamics have previously been identified in MoS₂,²⁰ WSe₂,^{19,23} and WS₂.¹ In the latter case, intervalley transfer time of 16 ± 5 *fs* was observed from temporal offsets of momentum-resolved signals via two-photon photoemission with > 50 *fs* temporal resolution. Here, we report on sub-100-*fs* formation of momentum-forbidden dark excitons in monolayer WS₂ measured directly (owing to the high temporal resolution) in a simpler setting (TR-PEEM) via one-photon photoemission. Taking advantage of imaging capabilities of the setup, we additionally distinguish spatially-heterogeneous signals from monolayer interior and edges, pointing at defects-mediated dynamics.

Methods

Sample preparation

Monolayers of WS₂ were grown on sapphire (Al₂O₃) substrate via chemical vapor deposition (CVD) following a similar procedure described previously.⁴⁰ For TR-PEEM experiments, the monolayers were subsequently transferred onto an *n*-doped silicon wafer with a natural oxide layer (SiO₂/*n*-Si).

Electronic-band-structure calculation

Electronic band structure of WS₂ monolayer was calculated using density functional theory (DFT) as implemented in Quantum Espresso.⁴¹

TR-PEEM experiment

Broadband visible excitation (pump) pulses (~ 10 fs duration, ~ 2 eV central energy, ~ 320 meV spectral bandwidth, 2.7–44 pJ energy per pulse) were generated in a lab-built non-collinear optical parametric amplifier (NOPA). Broadband deep-UV ionization (probe) pulses (~ 10 fs duration, ~ 4.7 eV central energy, ~ 330 meV spectral bandwidth, 7 pJ energy per pulse) were generated as second harmonic of the output (with 2.34 eV central energy) from a second NOPA via achromatic phase matching.^{38,39} Pulse repetition rate was 100 kHz. Both the excitation and ionization beams were weakly focused onto the sample inside the PEEM vacuum chamber at an angle of 25° with respect to the sample surface (Figure 1a). Both beams had ellipse-shaped spots on the sample surface with long and short axes being ~ 130 μm and ~ 80 μm (estimated fwhm) in the case of pump beam, and ~ 200 μm and ~ 50 μm in the case of probe beam, respectively. The pump and probe fluences at the sample were in the range of 8–136 nJ/cm² and 70 nJ/cm², respectively. The power in the probe beam was chosen low enough for samples not to degrade over the course of experiments²¹ as well as for images to be acquired without space charge effects,⁴² but sufficiently high to be able to

observe prominent pump-induced dynamics. Integration times during signal acquisition for each pump-probe delay were 40 *sec* (for 8 and 17 nJ/cm^2 pump), 20 *sec* (for 34 nJ/cm^2 pump), and 10 *sec* (for 136 nJ/cm^2 pump). During TR-PEEM experiments, samples were contained in ultrahigh vacuum ($\sim 10^{-10}$ *mbar*) inside a commercial PEEM apparatus (IS-PEEM, Focus GmbH) where electrons photoemitted from the sample ultimately formed an image on a charge-coupled device (CCD). The temporal and spatial resolution of the setup was estimated to be ~ 75 *nm* and ~ 13 *fs*, respectively (see Supplementary material, Sections S1,S2).

Results and discussion

Prior to measuring carrier dynamics in WS_2 monolayer, we first verified that the intensity of the pump beam was low enough for it alone not to cause high-order pump-induced photoemission from the flake (see Supplementary material, Section S3). For pump fluences used in our experiments, excitation density was estimated to be of the order of 10^{11} cm^{-2} which is three orders of magnitude lower than the Mott density.³ The energy of the probe pulses ultimately determined the photoemission horizon²¹ in the energy-momentum space (Figure 1b),

$$E_{probe} - W - E_b = \frac{\hbar k^2}{2m_e}, \quad (1)$$

beyond which no photoemission is possible. In Eq. (1), E_{probe} is probe pulse energy, W is workfunction of monolayer WS_2 , E_b is exciton binding energy, m_e is mass of electron, and k is in-plane momentum. As seen in Figure 1b, the detectable photoemission signal can only originate from the region (shaded blue) energetically-higher than the photoemission horizon covering momenta in the vicinity of Γ point of the Brillouin zone, so that the valleys at $\pm\Lambda$ points, which are energetically close to conduction band minima, can contribute photoemitted electrons via K-to- Λ intervalley scattering. Such scattering is expected to be enhanced in *n*-doped monolayers⁴³ leading to efficient generation of dark excitons. Addi-

tionally, likely presence of S-vacancies on the flake can result in mid-gap states $0.3\text{--}0.5\text{ eV}$ below the conduction band^{44,45} that can also fall into the probe region.

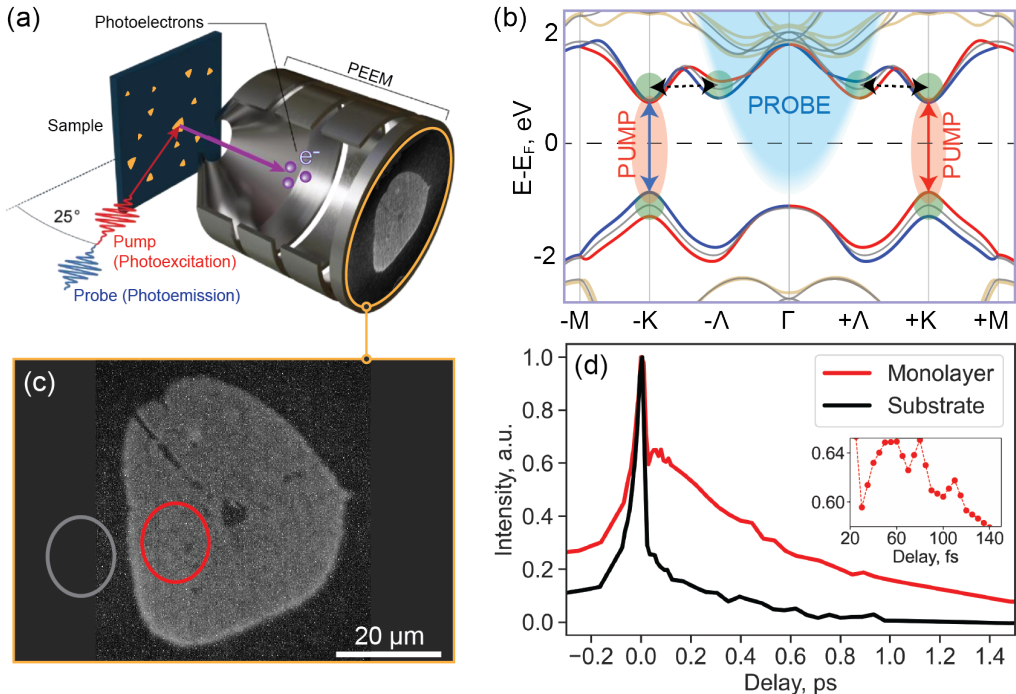


Figure 1: (a) A TR-PEEM experiment. Pump pulse (red) excites carriers in monolayer WS_2 (orange); probe pulse (blue) photoemits electrons from the monolayer; these electrons form an image (encircled with orange line) for each pump-probe delay. (b) Band structure of WS_2 monolayer calculated using DFT (Quantum Espresso⁴¹). Exciton transitions are indicated by blue and red arrows. Intervalley scattering is represented by dashed arrows. Area above photoemission horizon is shown shaded in blue with a Gaussian edge reflecting final duration of DUV pulses. (c) An image of a WS_2 monolayer flake obtained using a Hg (mercury) discharge lamp. The length of the scale-bar is $20\ \mu\text{m}$. Grey and red circles indicate areas, across which signals in (d) were integrated for each pump-probe delay. (d) Normalized pump-probe traces spatially-integrated across the monolayer-interior (red) and substrate (black) regions shown in (c). Pump and probe power densities were $136\ \text{nJ}/\text{cm}^2$ and $70\ \text{nJ}/\text{cm}^2$ per pulse, respectively, and integration time was 10 sec.

A photoemission image of a typical WS_2 monolayer flake is shown in Figure 1c. Similar flakes have been characterized previously^{46–48} revealing the energy of main exciton resonance of $\sim 2\text{ eV}$ and that of charged excitons (trions) a few tens of meV (charging energy) below. In TR-PEEM experiments reported here, the energy of pump pulses was tuned to overlap the

main exciton resonance thus promoting adiabatic exciton formation.^{1,20} The broad spectrum of the pump pulses also overlapped the energy of trions. The resulting coherent exciton polarization is expected to lose its coherence within 100 fs^{1,20} giving rise to incoherent excitons and trions. Pump-induced dynamics was then monitored via probe-induced photoemission. By construction of our experiment, TR-PEEM is sensitive to dark intervalley carriers inaccessible by conventional optical spectroscopies. Measured typical pump-probe traces from substrate and interior of monolayer WS₂ are shown in Figure 1d. Similar traces were also observed from other flakes on the substrate. In contrast to the substrate, monolayer WS₂ features a prominent well-resolved rise of photoemission signal on a sub-100-fs time scale.

Prior to the more-detailed analysis of the observed carrier dynamics, we assess whether substrate could potentially contribute photoemission background to the measured pump-probe signals across the monolayer flake. The work function of Si and SiO₂ have been previously reported to be 4.8 eV and 4.4 eV, respectively.⁴⁹ Given pump (2.0 eV) and probe (4.7 eV) energies used in this work, it is likely for substrate-electrons to be photoemitted from at least SiO₂ layer with excess energy E_e (electron kinetic energy) in the range of ~ 0.3 –2.3 eV. The de Broglie wavelength λ_e of such electrons is estimated as $\lambda_e = h/\sqrt{2m_e E_e}$ (m_e is electron’s mass, and h is Planck’s constant) yielding the values in the range of 0.81–1.22 nm, which are larger than the thickness ~ 0.6 nm of WS₂ monolayer.⁵⁰ Therefore, we, generally, expect a photoemission background from the substrate to contribute to the detected transient photoemission signals obtained from monolayer region. We thus use photoemission from the substrate as an estimate for such background and subtract it from the overall photoemission signal in a manner that naturally suppresses coherent exciton contributions in pump-probe traces (see Supplementary material, Section S4, for more details). The retrieved transient WS₂-specific photoemission contrast is shown in Figure 2. As expected, these differential dynamics feature delayed rise of photoemission signal followed by its subsequent decay. To gain more insights into the underlying carrier dynamics, we applied a simple fitting model to the resultant traces (see Supplementary material, Section S5), which takes into account

the finite rise of the detected signal,^{20,51}

$$I = \left(1 - e^{-\frac{\tau - \tau_0}{\tau_{rise}}}\right) \cdot \left(a_0 + a_1 e^{-\frac{\tau - \tau_0}{\tau_1}} + a_2 e^{-\frac{\tau - \tau_0}{\tau_2}}\right) \cdot H(\tau - \tau_0), \quad (2)$$

where τ_{rise} is the time-constant describing the sub-100-fs photoemission build-up; $\tau_{1,2}$ describe subsequent dynamics beyond 100 fs; $a_{1,2}$ are corresponding fitting amplitudes; a_0 and τ_0 are constant photoemission offset and time-zero calibration, respectively.

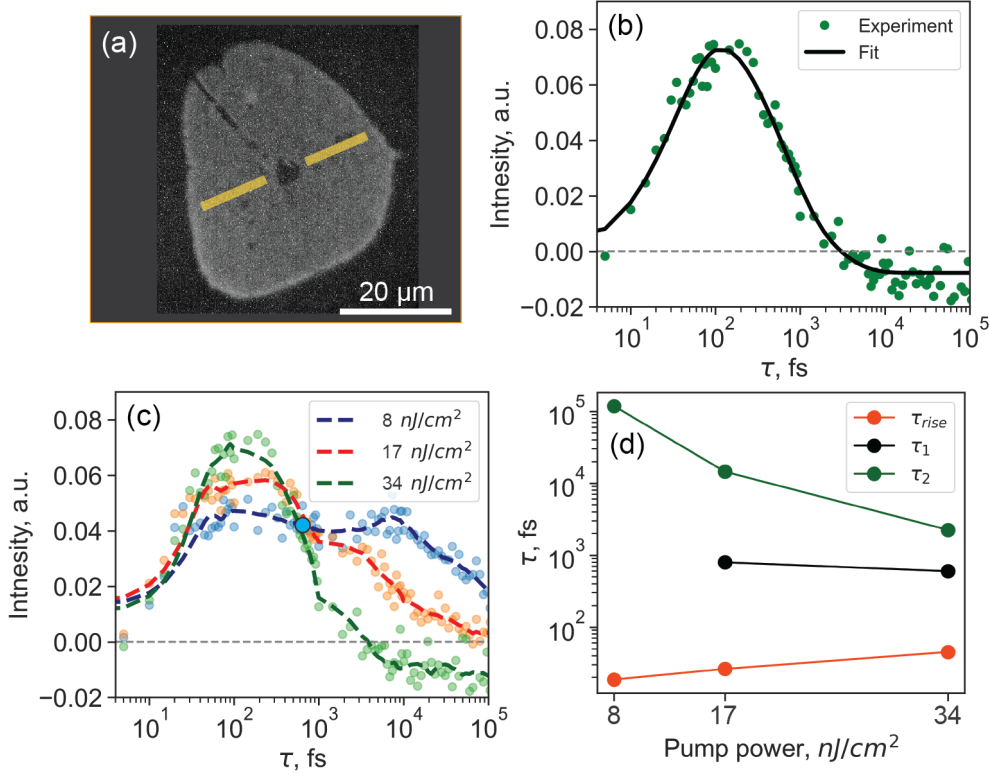


Figure 2: (a) Area (yellow), across which signal was integrated for analysis. (b) Fitting of the pump-probe trace obtained by integrating the pump-probe signal across the area (indicated in (a)) on WS₂ flake. Pump fluence was 34 nJ/cm². (c) Pump-probe traces from the same area as in (a) acquired for pump fluences of 8 (blue), 17 (red), and 34 (green) nJ/cm². Dashed lines reflect the result of smoothing to reveal fine details of the traces (see Supplementary material, Section S5, for the corresponding fittings). Isometric point is indicated by blue circle. (d) Power-dependence of extracted time-constants τ_{rise} (red), τ_1 (black), and τ_2 (green). The first τ_2 point is not shown since it is not representative of the second rising signal.

Figure 2b shows a result of fitting applied to a pump-probe trace obtained with 34 nJ/cm²

pump pulses, featuring a high fitting quality. We note a negative offset at longer delays indicating relative photoemission from the flake being less than that from the substrate, which is likely due to the effects of bandgap renormalization.^{52–55} Such renormalization could result in Λ -valleys lowering their energy below the photoemission horizon and/or a less energetically-favourable scattering to the probe region (if K-valleys become lower in energy than Λ -valleys). Regardless of these possible mechanisms, the net effect from both of them is the reduction in photoemission signal for higher pump fluences. Therefore, to provide a support for the hypothesis of the bandgap renormalization effects, we measured pump-induced photoemission for higher pump fluences resulting in even weaker photoemission signal (see Supplementary material, Section S6).

The retrieved time-constants are $\tau_{rise} \sim 45$ fs, $\tau_1 \sim 0.6$ ps, and $\tau_2 \sim 2.2$ ps. They are similar to those of previously-reported processes in 2D TMdC-based semiconductors, namely, (*rise*) exciton formation^{20,23} and K-to- Λ intervalley scattering,^{1,23} (*1,2*) reversal Λ -to-K intervalley scattering,²³ exciton decay,^{18,34} exciton-exciton annihilation,²³ and formation of trions.⁵¹ Due to very low excitation densities used in our experiments, we exclude exciton-exciton annihilation processes. Geminate exciton formation occurs outside the probe region and therefore should not contribute to photoemission either. In addition, it should be independent of pump fluence, but scattering processes are, in contrast, pump-fluence dependent. In the latter case, we note that for such low excitation densities used in this work, exciton-exciton scattering is not plausible intervalley transfer mechanism, and it is rather scattering mediated by phonons^{56,57} and/or plasmons⁵⁸ (due to intrinsic *n*-doping of CVD-grown monolayers⁵⁹) that would be at play in this case. To confirm scattering processes taking place and to gain a further insight into the detected sub-100-*fs* photoemission rise and subsequent dynamics, we acquired pump-fluence dependences of pump-probe signals (Figure 2c,d).

Figure 2c shows pump-probe dynamics measured for three pump fluences of 8 nJ/cm^2 , 17 nJ/cm^2 , and 34 nJ/cm^2 . Interestingly, fluence-dependent change of amplitudes occurs in opposite directions for delays shorter and longer than ~ 700 *fs*. Specifically, for delays

< 700 fs photoemission intensity overall increases with pump fluence, whereas for delays > 700 fs photoemission intensity decreases. This behaviour indicates a possible interplay of competing processes, which is also supported by the observation of a second rising signal (peaking at ~ 7 ps) most prominent in the pump-probe dynamics obtained with the lowest pump fluence of 8 nJ/cm². This observation points at a possible sequential carrier-transfer phenomenon that becomes more dominant for low pump fluences. The delay of ~ 700 fs, in this case, can be regarded as isometric point⁶⁰ in the temporal domain, *i.e.*, the point at which signal is independent of pump fluence (which is in agreement with nearly constant τ_2 for higher pump fluences). We note that the chosen model (Eq. (2)) fits well the two higher-fluence pump-probe traces, but does not take explicitly into account this secondary carrier transfer observed in the low-fluence case. Instead, by applying a fitting model that takes into account two rising and decaying signals (see Supplementary material, Section S7), we can obtain a better fit to the pump-probe trace for the lowest excitation density. In this case, signal rise times of $\tau_{rise,1} \sim 23.7$ fs and $\tau_{rise,2} \sim 1.1$ ps are retrieved, which are in agreement with the reported values of intervalley exciton scattering^{1,23} and trion formation,⁵¹ respectively. In Figure 2c, nevertheless, the fluence-dependent trends are extracted using the model described by Eq. (2) for consistency.

All three time-constants, overall, are fluence-dependent (Figure 2d) pointing at contributions of scattering-mediated processes, with τ_{rise} increasing, and τ_2 decreasing with pump fluence; the time-constant τ_1 initially increases and then decreases for increasing pump fluence (see Supplementary material, Section S5), which also supports an interplay of competing processes mentioned above. A lower scattering rate, as indicated by larger τ_{rise} , for larger pump-fluences further points at the above-mentioned likely additional effects of bandgap renormalization. The decreasing trend for τ_2 also additionally supports the above-mentioned second signal-rise wave, which in this case could reflect, indirectly, backscattering from Λ to K valleys or, directly, decay to longer-lived defect states (such as those introduced by S-vacancies) and/or generation of trions. To disentangle all these effects, further studies are

required. Provided discussion above, the time-constant τ_1 could reflect an interplay between exciton decay to lower states (such as traps and trions) within the probe region, and Λ -to-K carrier scattering away from the probe region. Thus, for lower fluences, it is the exciton decay to longer-lived states that is prevalent resulting in lower rates and prominent second rise of photoemission. For higher fluences, when bandgap renormalization takes place, energetically-lowered K-valleys could result in a more efficient backscattering.

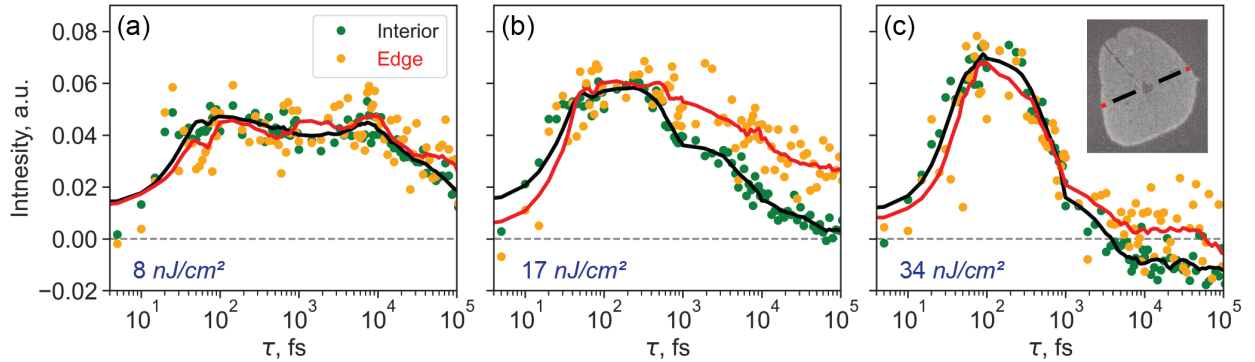


Figure 3: Comparison of pump-probe signals acquired from interior (green dots and black lines) and edges (orange dots and red lines) of the WS_2 flake for three excitation powers of (a) 8, (b) 17, and (c) 34 nJ/cm^2 . Solid lines represent the result of smoothing to reveal fine details of the traces. Signal integration areas are indicated in inset in (c).

We finally note that the measured carrier dynamics is most likely defects-mediated. It has been observed previously that edges in CVD-grown WS_2 monolayers contain larger amount of S-vacancies compared to the interior.^{44,61,62} Defect densities in the interior can be as large as $\sim 10^{13} \text{ cm}^{-2}$, whereas those near the edges of the order of $\sim 10^{14} \text{ cm}^{-2}$,⁴⁴ which are 2–3 orders of magnitude larger than excitation densities in this work (see also Ref.⁶¹). Owing to the high spatial resolution of the method, we can, in a straightforward way, recognize contributions from defect states to the detected response by comparing pump-probe dynamics from interior (with a lesser number of S-vacancies) and edges (with a larger density of S-vacancies) of the monolayer flake. Figure 3 shows pump-probe dynamics from interior and edges for the three investigated pump fluences. In all cases, a slower decay dynamics from the edges is evident confirming contributions from trap-mediated exciton dynamics across the flake. Notably, the intervalley scattering rates are not much different between the interior and edges of

monolayer flake (see Supplementary material, Section S5) indicating that defects likely do not act as efficient scattering centers in this case. Provided all the observed dynamics in this study, we conclude that dark excitons form within $\sim 14\text{--}50$ *fs* (within the range of set experimental conditions), matching the previously reported value.¹

Conclusion

In summary, we investigated intervalley carrier dynamics in monolayer WS₂ via PEEM coupled to a femtosecond pump-probe spectroscopy with very-high temporal resolution of 13 *fs*. We identified initial K-to- Λ intervalley scattering (formation of dark excitons) occurring on a time scale of 14–50 *fs*, depending on the excitation and defect density. The intervalley scattering does not appear to differ significantly between edges and interior of WS₂ monolayer. Subsequent dynamics suggested a decay of dark excitons to longer-lived states. Defects-mediated dynamics in this case was unambiguously identified by taking advantage of imaging capabilities of the apparatus with sub-diffraction-limited spatial resolution of 75 *nm*. The developed spectroscopy approach can be used for identification of sub-100-*fs* processes in other TMdC monolayers as well as graphene⁶³ and other topological semimetals.⁶⁴ Furthermore, complimenting ultrafast TR-PEEM method with excitation frequency resolution³⁰ and energy resolution of the photoemitted electrons will provide a more comprehensive picture of the ultrafast processes taking place in these materials.

Acknowledgements

The work was supported by Vetenskapsrådet, Crafoordska Stiftelsen, and NanoLund. M.S.F. acknowledges support from the Australian Research Council (DP200101345 and CE170100039).

Authors disclosure statement

Authors declare no competing financial interests.

Supporting Information Available

The following file is available as Supplementary material:

- supplementary.pdf

References

1. Wallauer, R.; Perea-Causin, R.; Münster, L.; Zajusch, S.; Brem, S.; Gütde, J.; Tanimura, K.; Lin, K.-Q.; Huber, R.; Malic, E.; Höfer, U. Momentum-Resolved Observation of Exciton Formation Dynamics in Monolayer WS₂. *Nano Letters* **2021**, *21*, 5867–5873.
2. Mueller, T.; Malic, E. Exciton physics and device application of two-dimensional transition metal dichalcogenide semiconductors. *npj 2D Materials and Applications* **2018**, *2*, 29.
3. Chernikov, A.; Ruppert, C.; Hill, H. M.; Rigosi, A. F.; Heinz, T. F. Population inversion and giant bandgap renormalization in atomically thin WS₂ layers. *Nature Photonics* **2015**, *9*, 466–470.
4. Splendiani, A.; Sun, L.; Zhang, Y.; Li, T.; Kim, J.; Chim, C.-Y.; Galli, G.; Wang, F. Emerging Photoluminescence in Monolayer MoS₂. *Nano Letters* **2010**, *10*, 1271–1275.
5. Mak, K. F.; He, K.; Lee, C.; Lee, G. H.; Hone, J.; Heinz, T. F.; Shan, J. Tightly bound trions in monolayer MoS₂. *Nature Materials* **2012**, *12*, 207–211.
6. You, Y.; Zhang, X.-X.; Berkelbach, T. C.; Hybertsen, M. S.; Reichman, D. R.; Heinz, T. F. Observation of biexcitons in monolayer WSe₂. *Nature Physics* **2015**, *11*, 477–481.

7. Hao, K.; Specht, J. F.; Nagler, P.; Xu, L.; Tran, K.; Singh, A.; Dass, C. K.; Schüller, C.; Korn, T.; Richter, M.; Knorr, A.; Li, X.; Moody, G. Neutral and charged inter-valley biexcitons in monolayer MoSe₂. *Nature Communications* **2017**, *8*, 15552.
8. Sie, E. J.; Frenzel, A. J.; Lee, Y.-H.; Kong, J.; Gedik, N. Intervalley biexcitons and many-body effects in monolayer MoS₂. *Physical Review B* **2015**, *92*, 125417.
9. Kogar, A.; Rak, M. S.; Vig, S.; Husain, A. A.; Flicker, F.; Joe, Y. I.; Venema, L.; MacDougall, G. J.; Chiang, T. C.; Fradkin, E.; van Wezel, J.; Abbamonte, P. Signatures of exciton condensation in a transition metal dichalcogenide. *Science* **2017**, *358*, 1314–1317.
10. Sun, B.; Zhao, W.; Palomaki, T.; Fei, Z.; Runburg, E.; Malinowski, P.; Huang, X.; Cenker, J.; Cui, Y.-T.; Chu, J.-H.; Xu, X.; Ataei, S. S.; Varsano, D.; Palummo, M.; Molinari, E.; Rontani, M.; Cobden, D. H. Evidence for equilibrium exciton condensation in monolayer WTe₂. *Nature Physics* **2021**, *18*, 94–99.
11. Li, J.; Goryca, M.; Choi, J.; Xu, X.; Crooker, S. A. Many-Body Exciton and Intervalley Correlations in Heavily Electron-Doped WSe₂ Monolayers. *Nano Letters* **2021**, *22*, 426–432.
12. Xiao, K.; Yan, T.; Liu, Q.; Yang, S.; Kan, C.; Duan, R.; Liu, Z.; Cui, X. Many-Body Effect on Optical Properties of Monolayer Molybdenum Diselenide. *The Journal of Physical Chemistry Letters* **2021**, *12*, 2555–2561.
13. Chernikov, A.; Berkelbach, T. C.; Hill, H. M.; Rigosi, A.; Li, Y.; Aslan, B.; Reichman, D. R.; Hybertsen, M. S.; Heinz, T. F. Exciton Binding Energy and Nonhydrogenic Rydberg Series in Monolayer WS₂. *Physical Review Letters* **2014**, *113*, 076802.
14. Su, H.; Xu, D.; Cheng, S.-W.; Li, B.; Liu, S.; Watanabe, K.; Taniguchi, T.; Berkelbach, T. C.; Hone, J. C.; Delor, M. Dark-Exciton Driven Energy Funneling into Di-

- electric Inhomogeneities in Two-Dimensional Semiconductors. *Nano Letters* **2022**, *22*, 2843–2850.
15. Lin, J.-D.; Lo, P.-Y.; Peng, G.-H.; Li, W.-H.; Huang, S.-Y.; Chen, G.-Y.; Cheng, S.-J. Essential role of momentum-forbidden dark excitons in the energy transfer responses of monolayer transition-metal dichalcogenides. *npj 2D Materials and Applications* **2023**, *7*, 51.
 16. Chand, S. B.; Woods, J. M.; Quan, J.; Mejia, E.; Taniguchi, T.; Watanabe, K.; Alù, A.; Grosso, G. Interaction-driven transport of dark excitons in 2D semiconductors with phonon-mediated optical readout. *Nature Communications* **2023**, *14*, 3712.
 17. Katzer, M.; Kovalchuk, S.; Greben, K.; Bolotin, K. I.; Selig, M.; Knorr, A. Impact of dark excitons on Förster-type resonant energy transfer between dye molecules and atomically thin semiconductors. *Physical Review B* **2023**, *107*, 035304.
 18. Ceballos, F.; Cui, Q.; Bellus, M. Z.; Zhao, H. Exciton formation in monolayer transition metal dichalcogenides. *Nanoscale* **2016**, *8*, 11681–11688.
 19. Steinleitner, P.; Merkl, P.; Nagler, P.; Mornhinweg, J.; Schüller, C.; Korn, T.; Chernikov, A.; Huber, R. Direct Observation of Ultrafast Exciton Formation in a Monolayer of WSe₂. *Nano Letters* **2017**, *17*, 1455–1460.
 20. Trovatiello, C.; Katsch, F.; Borys, N. J.; Selig, M.; Yao, K.; Borrego-Varillas, R.; Scotognella, F.; Kriegel, I.; Yan, A.; Zettl, A.; Schuck, P. J.; Knorr, A.; Cerullo, G.; Conte, S. D. The ultrafast onset of exciton formation in 2D semiconductors. *Nature Communications* **2020**, *11*, 5277.
 21. Li, Y.; Liu, W.; Wang, Y.; Xue, Z.; Leng, Y.-C.; Hu, A.; Yang, H.; Tan, P.-H.; Liu, Y.; Misawa, H.; Sun, Q.; Gao, Y.; Hu, X.; Gong, Q. Ultrafast Electron Cooling and Decay in Monolayer WS₂ Revealed by Time- and Energy-Resolved Photoemission Electron Microscopy. *Nano Letters* **2020**, *20*, 3747–3753.

22. Hein, P.; Stange, A.; Hanff, K.; Yang, L. X.; Rohde, G.; Rossnagel, K.; Bauer, M. Momentum-resolved hot electron dynamics at the $2H$ -MoS₂ surface. *Physical Review B* **2016**, *94*, 205406.
23. Wang, L.; Xu, C.; Li, M.-Y.; Li, L.-J.; Loh, Z.-H. Unraveling Spatially Heterogeneous Ultrafast Carrier Dynamics of Single-Layer WSe₂ by Femtosecond Time-Resolved Photoemission Electron Microscopy. *Nano Letters* **2018**, *18*, 5172–5178.
24. Bao, D.; del Águila, A. G.; Thu Ha Do, T.; Liu, S.; Pei, J.; Xiong, Q. Probing momentum-indirect excitons by near-resonance photoluminescence excitation spectroscopy in WS₂ monolayer. *2D Materials* **2020**, *7*, 031002.
25. Sun, D.; Rao, Y.; Reider, G. A.; Chen, G.; You, Y.; Brézin, L.; Harutyunyan, A. R.; Heinz, T. F. Observation of Rapid Exciton–Exciton Annihilation in Monolayer Molybdenum Disulfide. *Nano Letters* **2014**, *14*, 5625–5629.
26. Erkensten, D.; Brem, S.; Wagner, K.; Gillen, R.; Perea-Causín, R.; Ziegler, J. D.; Taniguchi, T.; Watanabe, K.; Maultzsch, J.; Chernikov, A.; Malic, E. Dark exciton–exciton annihilation in monolayer WSe₂. *Physical Review B* **2021**, *104*, 1241406.
27. Lee, Y.; Tran, T. T.; Kim, Y.; Roy, S.; Taniguchi, T.; Watanabe, K.; Jang, J. I.; Kim, J. Enhanced Radiative Exciton Recombination in Monolayer WS₂ on the hBN Substrate Competing with Nonradiative Exciton–Exciton Annihilation. *ACS Photonics* **2022**, *9*, 873–879.
28. Herman, A. P.; Zelewski, S. J.; Misztal, K.; Kudrawiec, R. Probing the long-lived photo-generated charge carriers in transition metal dichalcogenides by time-resolved microwave photoconductivity. *Nanophotonics* **2022**, *11*, 1335–1344.
29. Reding, J.; Zhang, W.; Allam, J. Imaging Excited-State Dynamics in Two-Dimensional Semiconductors with Emerging Ultrafast Measurement Techniques. *Accounts of Materials Research* **2021**, *2*, 75–85.

30. Huber, B.; Pres, S.; Wittmann, E.; Dietrich, L.; Lüttig, J.; Fersch, D.; Krauss, E.; Friedrich, D.; Kern, J.; Lisinetskii, V.; Hensen, M.; Hecht, B.; Bratschitsch, R.; Riedle, E.; Brixner, T. Space- and time-resolved UV-to-NIR surface spectroscopy and 2D nanoscopy at 1 MHz repetition rate. *Review of Scientific Instruments* **2019**, *90*, 113103.
31. Xu, C.; Yong, H. W.; He, J.; Long, R.; Cadore, A. R.; Paradisanos, I.; Ott, A. K.; Soavi, G.; Tongay, S.; Cerullo, G.; Ferrari, A. C.; Prezhdov, O. V.; Loh, Z.-H. Weak Distance Dependence of Hot-Electron-Transfer Rates at the Interface between Monolayer MoS₂ and Gold. *ACS Nano* **2020**, *15*, 819–828.
32. Sass, P. M.; El-Khoury, P. Z. Femtosecond-Nanometer Visualization of Exciton Dynamics in MoSe₂. *arXiv* **2021**, 2109.12089.
33. Liang, Y.; Li, B.-H.; Li, Z.; Zhang, G.; Sun, J.; Zhou, C.; Tao, Y.; Ye, Y.; Ren, Z.; Yang, X. Spatially heterogeneous ultrafast interfacial carrier dynamics of 2D-MoS₂ flakes. *Materials Today Physics* **2021**, *21*, 100506.
34. Madéo, J.; Man, M. K. L.; Sahoo, C.; Campbell, M.; Pareek, V.; Wong, E. L.; Al-Mahboob, A.; Chan, N. S.; Karmakar, A.; Mariserla, B. M. K.; Li, X.; Heinz, T. F.; Cao, T.; Dani, K. M. Directly visualizing the momentum-forbidden dark excitons and their dynamics in atomically thin semiconductors. *Science* **2020**, *370*, 1199–1204.
35. Helmrich, S.; Sampson, K.; Huang, D.; Selig, M.; Hao, K.; Tran, K.; Achstein, A.; Young, C.; Knorr, A.; Malic, E.; Woggon, U.; Owschimikow, N.; Li, X. Phonon-Assisted Intervalley Scattering Determines Ultrafast Exciton Dynamics in MoSe₂ Bilayers. *Physical Review Letters* **2021**, *127*, 157403.
36. Bertoni, R.; Nicholson, C.; Waldecker, L.; Hübener, H.; Monney, C.; Giovannini, U. D.; Puppini, M.; Hoesch, M.; Springate, E.; Chapman, R.; Cacho, C.; Wolf, M.; Rubio, A.; Ernstorfer, R. Generation and Evolution of Spin-, Valley-, and Layer-Polarized Excited Carriers in Inversion-Symmetric WSe₂. *Physical Review Letters* **2016**, *117*, 277201.

37. Dong, S.; Puppini, M.; Pincelli, T.; Beaulieu, S.; Christiansen, D.; Hübener, H.; Nicholson, C. W.; Xian, R. P.; Dendzik, M.; Deng, Y.; Windsor, Y. W.; Selig, M.; Malic, E.; Rubio, A.; Knorr, A.; Wolf, M.; Rettig, L.; Ernstorfer, R. Direct measurement of key exciton properties: Energy, dynamics, and spatial distribution of the wave function. *Natural Sciences* **2021**, *1*, e10010.
38. Baum, P.; Lochbrunner, S.; Riedle, E. Tunable sub-10-fs ultraviolet pulses generated by achromatic frequency doubling. *Optics Letters* **2004**, *29*, 1686.
39. Bruder, L.; Wittenbecher, L.; Kolesnichenko, P. V.; Zigmantas, D. Generation and compression of 10-fs deep ultraviolet pulses at high repetition rate using standard optics. *Optics Express* **2021**, *29*, 25593.
40. Zhang, Q.; Lu, J.; Wang, Z.; Dai, Z.; Zhang, Y.; Huang, F.; Bao, Q.; Duan, W.; Fuhrer, M. S.; Zheng, C. Reliable Synthesis of Large-Area Monolayer WS₂ Single Crystals, Films, and Heterostructures with Extraordinary Photoluminescence Induced by Water Intercalation. *Advanced Optical Materials* **2018**, *6*, 1701347.
41. Giannozzi, P.; Baroni, S.; Bonini, N.; Calandra, M.; Car, R.; Cavazzoni, C.; Ceresoli, D.; Chiarotti, G. L.; Cococcioni, M.; Dabo, I.; Dal Corso, A.; de Gironcoli, S.; Fabris, S.; Fratesi, G.; Gebauer, R.; Gerstmann, U.; Gougoussis, C.; Kokalj, A.; Lazzeri, M.; Martin-Samos, L. *et al.* QUANTUM ESPRESSO: a modular and open-source software project for quantum simulations of materials. *Journal of Physics: Condensed Matter* **2009**, *21*, 395502.
42. Buckanie, N. M.; Göhre, J.; Zhou, P.; von der Linde, D.; Horn-von Hoegen, M.; Meyer zu Heringdorf, F.-J. Space charge effects in photoemission electron microscopy using amplified femtosecond laser pulses. *Journal of Physics: Condensed Matter* **2009**, *21*, 314003.
43. Pei, J.; Liu, X.; del Águila, A. G.; Bao, D.; Liu, S.; Amara, M.-R.; Zhao, W.; Zhang, F.; You, C.; Zhang, Y.; Watanabe, K.; Taniguchi, T.; Zhang, H.; Xiong, Q. Switching of

- K-Q intervalley trions fine structure and their dynamics in n-doped monolayer WS₂. *Opto-Electronic Advances* **2023**, *6*, 220034–220034.
44. Carozo, V.; Wang, Y.; Fujisawa, K.; Carvalho, B. R.; McCreary, A.; Feng, S.; Lin, Z.; Zhou, C.; Perea-López, N.; Elías, A. L.; Kabius, B.; Crespi, V. H.; Terrones, M. Optical identification of sulfur vacancies: Bound excitons at the edges of monolayer tungsten disulfide. *Science Advances* **2017**, *3*, e160281.
45. Gao, C.; Yang, X.; Jiang, M.; Chen, L.; Chen, Z.; Singh, C. V. Synergistic vacancy defects and mechanical strain for the modulation of the mechanical, electronic and optical properties of monolayer tungsten disulfide. *Physical Chemistry Chemical Physics* **2021**, *23*, 6298–6308.
46. Kolesnichenko, P. V.; Zhang, Q.; Yun, T.; Zheng, C.; Fuhrer, M. S.; Davis, J. A. Disentangling the effects of doping, strain and disorder in monolayer WS₂ by optical spectroscopy. *2D Materials* **2020**, *7*, 025008.
47. Kolesnichenko, P. V.; Zhang, Q.; Zheng, C.; Fuhrer, M. S.; Davis, J. A. Multidimensional analysis of excitonic spectra of monolayers of tungsten disulphide: toward computer-aided identification of structural and environmental perturbations of 2D materials. *Machine Learning: Science and Technology* **2021**, *2*, 025021.
48. McCreary, K. M.; Hanbicki, A. T.; Singh, S.; Kawakami, R. K.; Jernigan, G. G.; Ishigami, M.; Ng, A.; Brintlinger, T. H.; Stroud, R. M.; Jonker, B. T. The Effect of Preparation Conditions on Raman and Photoluminescence of Monolayer WS₂. *Scientific Reports* **2016**, *6*, 35154.
49. Lindmayer, J. Field effect studies of the oxidized silicon surface. *Solid-State Electronics* **1966**, *9*, 225–235.
50. Okada, M.; Okada, N.; Chang, W.-H.; Endo, T.; Ando, A.; Shimizu, T.; Kubo, T.;

- Miyata, Y.; Irisawa, T. Gas-Source CVD Growth of Atomic Layered WS₂ from WF₆ and H₂S Precursors with High Grain Size Uniformity. *Scientific Reports* **2019**, *9*, 17678.
51. Singh, A.; Moody, G.; Tran, K.; Scott, M. E.; Overbeck, V.; Berghäuser, G.; Schaibley, J.; Seifert, E. J.; Pleskot, D.; Gabor, N. M.; Yan, J.; Mandrus, D. G.; Richter, M.; Malic, E.; Xu, X.; Li, X. Trion formation dynamics in monolayer transition metal dichalcogenides. *Physical Review B* **2016**, *93*, 041401(R).
52. Wang, Q.; Ge, S.; Li, X.; Qiu, J.; Ji, Y.; Feng, J.; Sun, D. Valley Carrier Dynamics in Monolayer Molybdenum Disulfide from Helicity-Resolved Ultrafast Pump-Probe Spectroscopy. *ACS Nano* **2013**, *7*, 11087–11093.
53. Pogna, E. A. A.; Marsili, M.; De Fazio, D.; Dal Conte, S.; Manzoni, C.; Sangalli, D.; Yoon, D.; Lombardo, A.; Ferrari, A. C.; Marini, A.; Cerullo, G.; Prezzi, D. Photo-Induced Bandgap Renormalization Governs the Ultrafast Response of Single-Layer MoS₂. *ACS Nano* **2016**, *10*, 1182–1188.
54. Cunningham, P. D.; Hanbicki, A. T.; McCreary, K. M.; Jonker, B. T. Photoinduced Bandgap Renormalization and Exciton Binding Energy Reduction in WS₂. *ACS Nano* **2017**, *11*, 12601–12608.
55. Lin, T. N.; Santiago, S. R. M.; Caigas, S. P.; Yuan, C. T.; Lin, T. Y.; Shen, J. L.; Chen, Y. F. Many-body effects in doped WS₂ monolayer quantum disks at room temperature. *npj 2D Materials and Applications* **2019**, *3*, 46.
56. Christiansen, D.; Selig, M.; Berghäuser, G.; Schmidt, R.; Niehues, I.; Schneider, R.; Arora, A.; de Vasconcellos, S. M.; Bratschitsch, R.; Malic, E.; Knorr, A. Phonon Sidebands in Monolayer Transition Metal Dichalcogenides. *Physical Review Letters* **2017**, *119*, 187402.
57. Raja, A.; Selig, M.; Berghäuser, G.; Yu, J.; Hill, H. M.; Rigosi, A. F.; Brus, L. E.;

- Knorr, A.; Heinz, T. F.; Malic, E.; Chernikov, A. Enhancement of Exciton–Phonon Scattering from Monolayer to Bilayer WS₂. *Nano Letters* **2018**, *18*, 6135–6143.
58. Van Tuan, D.; Scharf, B.; Žutić, I.; Dery, H. Marrying Excitons and Plasmons in Monolayer Transition-Metal Dichalcogenides. *Physical Review X* **2017**, *7*, 041040.
59. Chae, W. H.; Cain, J. D.; Hanson, E. D.; Murthy, A. A.; Dravid, V. P. Substrate-induced strain and charge doping in CVD-grown monolayer MoS₂. *Applied Physics Letters* **2017**, *111*, 143106.
60. Kaspar, F. Quality Data from Messy Spectra: How Isometric Points Increase Information Content in Highly Overlapping Spectra. *ChemBioChem* **2023**, *24*, e2022007.
61. Bao, W.; Borys, N. J.; Ko, C.; Suh, J.; Fan, W.; Thron, A.; Zhang, Y.; Buyanin, A.; Zhang, J.; Cabrini, S.; Ashby, P. D.; Weber-Bargioni, A.; Tongay, S.; Aloni, S.; Ogle-tree, D. F.; Wu, J.; Salmeron, M. B.; Schuck, P. J. Visualizing nanoscale excitonic relaxation properties of disordered edges and grain boundaries in monolayer molybdenum disulfide. *Nature Communications* **2015**, *6*, 7993.
62. Rosenberger, M. R.; Chuang, H.-J.; McCreary, K. M.; Li, C. H.; Jonker, B. T. Electrical Characterization of Discrete Defects and Impact of Defect Density on Photoluminescence in Monolayer WS₂. *ACS Nano* **2018**, *12*, 1793–1800.
63. Trepalin, V.; Asselberghs, I.; Brems, S.; Huyghebaert, C.; Radu, I.; Afanas'ev, V.; Houssa, M.; Stesmans, A. Evaluation of the effective work-function of monolayer graphene on silicon dioxide by internal photoemission spectroscopy. *Thin Solid Films* **2019**, *674*, 39–43.
64. Biswal, B.; Mishra, S. B.; Yadav, R.; Poudyal, S.; Rajarapu, R.; Barman, P. K.; Pandurang, K. R.; Mandal, M.; Singh, R. P.; Nanda, B. R. K.; Misra, A. Work function of van der Waals topological semimetals: Experiment and theory. *Applied Physics Letters* **2022**, *120*, 093101.

Supplementary material to: "Sub-100-fs formation of dark excitons in monolayer WS₂"

Pavel V. Kolesnichenko,^{*,†,‡} Lukas Wittenbecher,[¶] Qianhui Zhang,[⊥] Run Yan Teh,[#] Chandni Babu,[§] Michael S. Fuhrer,^{@,△} Anders Mikkelsen,[¶] and Donatas Zigmantas^{*,§}

[†]*Institute of Physical Chemistry, Heidelberg University, 69120, Heidelberg, Germany*

[‡]*Institute for Molecular Systems, Engineering and Advanced Materials, Heidelberg University, 69120, Heidelberg, Germany*

[¶]*Department of Physics, Lund University, Box 118, 221 00 Lund, Sweden*

[§]*Division of Chemical Physics, Lund University, P.O. Box 124, 221 00 Lund, Sweden*

^{||}*NanoLund, P.O. Box 124, 221 00 Lund, Sweden*

[⊥]*Department of Civil Engineering, Monash University, Melbourne, Victoria 3800, Australia*

[#]*Centre for Quantum Science and Technology Theory, Swinburne University of Technology, Melbourne, Victoria 3122, Australia*

[@]*School of Physics and Astronomy, Monash University, Melbourne, Victoria 3800, Australia*

[△]*ARC Centre of Excellence in Future Low-Energy Electronics Technologies, Monash University, Melbourne, Victoria 3800 Australia*

E-mail: pavel.kolesnichenko@alumni.uni-heidelberg.de; donatas.zigmantas@chemphys.lu.se

S1. Pulse spectra and time-resolution of TR-PEEM

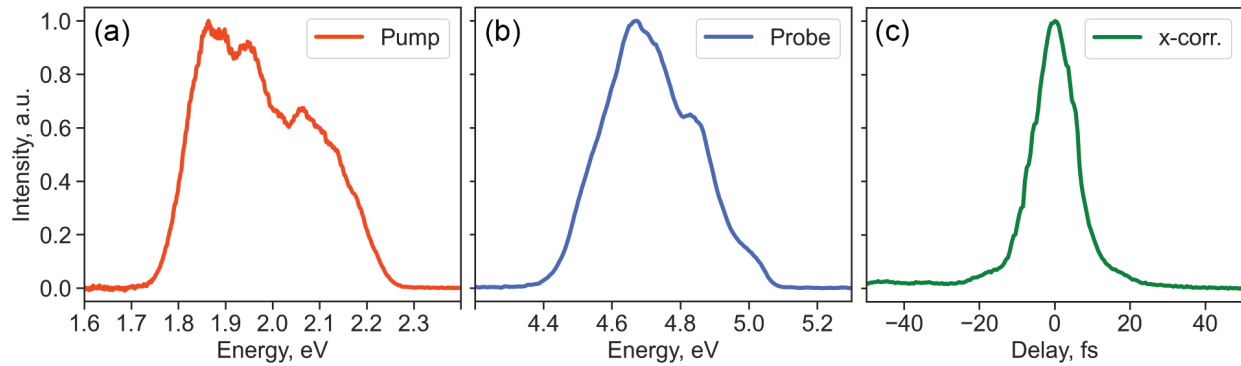


Figure S1: (a) Pump and (b) probe spectra, and (c) temporal cross-correlation (x-corr.) of pump and probe pulses measured via pump-induced transient-grating gate in a thin fused silica plate.¹ The x-corr. was measured in front of the PEEM's input window taking the window material into account. The fwhm of x-corr. profile is 13.4 fs defining temporal resolution of the TR-PEEM apparatus.

S2. Spatial resolution of TR-PEEM

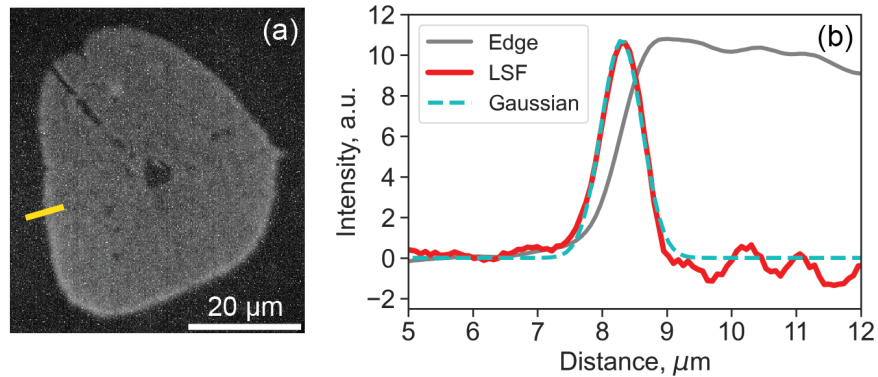


Figure S2: (a) Monolayer WS₂ flake imaged via a mercury lamp. (b) Edge profile (grey) taken along the yellow line indicated in (a), line spread function (LSF, red) of the edge profile, and a Gaussian fit to LSF with fwhm of 74.6 nm defining spatial resolution of the TR-PEEM apparatus.

S3. Pump-induced excitation and photoemission

Table S1: Pump fluences and corresponding carrier excitation densities.

Pump fluence, nJ/cm^2	8	17	34	136
Excitation density, $10^{11} \times cm^{-2}$	0.52	1.05	2.12	8.49

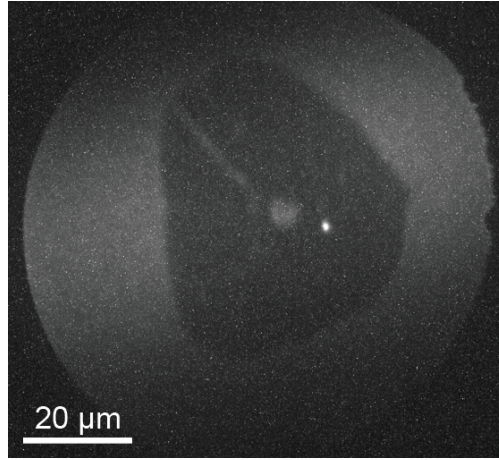


Figure S3: A photoemission image of the WS_2 monolayer flake obtained using $136 \text{ nJ}/\text{cm}^{-2}$ pump pulses (with probe pulses blocked).

S4. Monolayer-specific dynamics

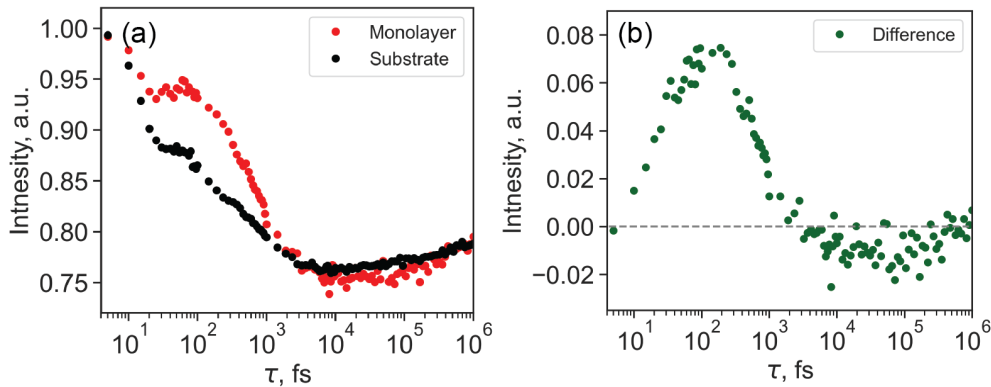


Figure S4: (a) Normalization of raw pump-probe traces obtained from WS_2 monolayer interior and substrate. (b) Difference (also Figure 2a of the main text) between the pump-probe traces in (a). Pump fluence was $34 \text{ nJ}/\text{cm}^2$.

The two spectra were pinned at 0 fs and 1 ns delays (Figure S4a) and subtracted (Figure S4b). This procedure naturally suppresses the effects from pulse overlap including coherent exciton population signal.

S5. Fittings of pump-probe traces

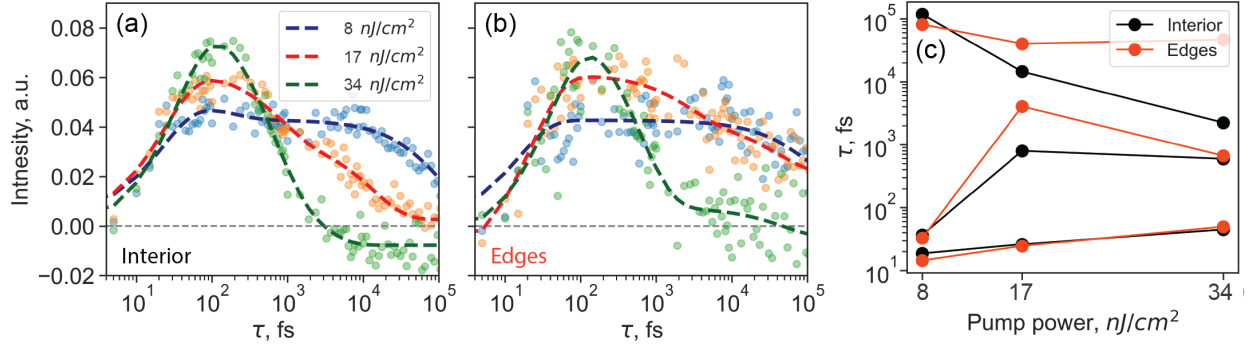


Figure S5: Fittings of the pump-probe traces shown in Figure 2b of the main text.

Table S2: Extracted time-constants for the three pump fluences (interior of the flake)

	8 nJ/cm^2	17 nJ/cm^2	34 nJ/cm^2
τ_{rise}, fs	18.7	26.3	45.1
τ_1, fs	36.9	797	596
τ_2, ps	118.2	14.5	2.2

Table S3: Extracted time-constants for the three pump fluences (flake's edges)

	8 nJ/cm^2	17 nJ/cm^2	34 nJ/cm^2
τ_{rise}, fs	14.5	24.6	50.0
τ_1, fs	32.7	2747	624
τ_2, ps	81.6	40.2	46.6

S6. Photoemission contrast drop for higher pump fluences

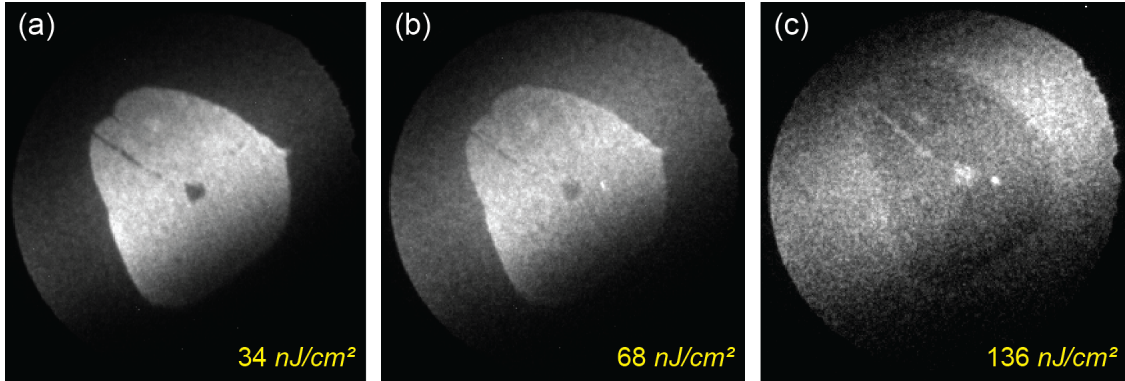


Figure S6: Photoemission at 7 ps pump-probe delay for three pump fluences of (a) 34 nJ/cm^2 , (b) 68 nJ/cm^2 , and (c) 136 nJ/cm^2 . For higher fluences photoemission contrast from the flake becomes lower.

S7. Fitting with two rise-and-decay signals

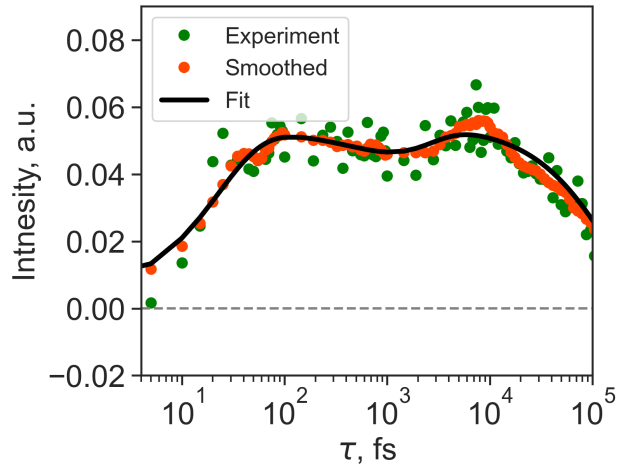


Figure S7: Fitting with a model (Eq. (S1)) accounting for two rise-and-decay signals. Pump fluence is 8 nJ/cm^2 .

Extracted rise time-constants are $\tau_{rise,1} \sim 23.7 \text{ fs}$ and $\tau_{rise,2} \sim 1.1 \text{ ps}$ comparable to

previously reported values of dark-exciton^{2,3} and trion formation.⁴

$$I = \left((1 - a_{rise,1} e^{-\frac{\tau - \tau_{0,1}}{\tau_{rise,1}}}) \cdot a_1 e^{-\frac{\tau - \tau_{0,1}}{\tau_1}} + (1 - a_{rise,2} e^{-\frac{\tau - \tau_{0,2}}{\tau_{rise,2}}}) \cdot a_2 e^{-\frac{\tau - \tau_{0,2}}{\tau_2}} + a_0 \right) \cdot H(\tau - \tau_0) \quad (\text{S1})$$

References

1. Bruder, L.; Wittenbecher, L.; Kolesnichenko, P. V.; Zigmantas, D. Generation and compression of 10-fs deep ultraviolet pulses at high repetition rate using standard optics. *Optics Express* **2021**, *29*, 25593.
2. Wang, L.; Xu, C.; Li, M.-Y.; Li, L.-J.; Loh, Z.-H. Unraveling Spatially Heterogeneous Ultrafast Carrier Dynamics of Single-Layer WSe₂ by Femtosecond Time-Resolved Photoemission Electron Microscopy. *Nano Letters* **2018**, *18*, 5172–5178.
3. Wallauer, R.; Perea-Causin, R.; Münster, L.; Zajusch, S.; Brem, S.; Gütde, J.; Tanimura, K.; Lin, K.-Q.; Huber, R.; Malic, E.; Höfer, U. Momentum-Resolved Observation of Exciton Formation Dynamics in Monolayer WS₂. *Nano Letters* **2021**, *21*, 5867–5873.
4. Singh, A.; Moody, G.; Tran, K.; Scott, M. E.; Overbeck, V.; Berghäuser, G.; Schaibley, J.; Seifert, E. J.; Pleskot, D.; Gabor, N. M.; Yan, J.; Mandrus, D. G.; Richter, M.; Malic, E.; Xu, X.; Li, X. Trion formation dynamics in monolayer transition metal dichalcogenides. *Physical Review B* **2016**, *93*, 041401(R).